minerals

Article

# U–Pb Dating and Trace Element Composition of Zircons from the Gujiao Ore-Bearing Intrusion, Shanxi, China: Implications for Timing and Mineralization of the Guojialiang Iron Skarn Deposit

**Ze-Guang Chang [1], Guo-Chen Dong [1,*] and Alireza K. Somarin [2]**

[1] School of Earth Sciences and Resources, China University of Geosciences Beijing, 29 Xueyuan Road, Beijing 100083, China; 3001180010@cugb.edu.cn
[2] Department of Geology, Brandon University, Brandon, MB R7A 6A9, Canada; somarina@brandonu.ca
* Correspondence: donggc@cugb.edu.cn

Received: 7 December 2019; Accepted: 1 January 2020; Published: 31 March 2020

**Abstract:** The Gujiao ore field, located in the middle segment of the Lüliang Mountain in central North China Craton (NCC), is one of iron skarn deposits of western iron belt in China. The U–Pb dating results of zircon by LA-ICP-MS suggest that the ore-related monzonite from the Guojialiang deposit was formed at 129.7 ± 1.7 Ma, early Cretaceous, which is consistent with the timing of iron skarn deposits in the Handan–Xingtai district of western iron belt. The zircons of monzonite present notable positive Ce anomalies (Ce/Ce* = 23.38–45.85), high $Ce^{4+}/Ce^{3+}$ values (154–385) and relatively high oxygen fugacity ($fO_2$ = −13.09 to −15.36), and yield relatively low Ti-in-zircon temperatures. The physico-chemical conditions of the Guojialiang deposit were quite similar to these of ore-bearing plutons in the Handan-Xingtai district. The ore-bearing magmas are derived from the enriched lithospheric mantle with crustal material contribution, which played key role in oxidation state of the magma and the iron mineralization in the western iron belt.

**Keywords:** iron skarn deposit; zircon U–Pb dating; oxygen fugacity; ore mineralization

## 1. Introduction

The North China Craton (NCC) has experienced reactivation or decratonization during the Late Mesozoic [1–3], accompanied by large-scale magmatism and endogenic mineralization [4–9]. The skarn-type iron deposit is one such mineralization type that has provided a crucial source of high-grade iron ores, especially in China [10]. Despite a majority of skarn-type iron deposits being associated with arc setting [11], the Mesozoic skarn Fe deposits in the NCC were generated within an intraplate extensional setting [8]. The iron skarn deposits are mainly distributed in the central-eastern NCC and roughly form two belts, eastern iron skarn deposit belt and western iron skarn deposit belt (Figure 1a) [12]. The western iron skarn deposit belt consists of the Southern Taihang district ore deposit cluster, Gujiao (or Taiyuan) ore field, and Linfen ore field (Figure 1a). All these iron deposits in the western belt have similar ore-related intrusive rocks, monzonites, and/or diorites, and similar country rocks: Middle Ordovician marine carbonate rocks. The age, geological features, and metallogenesis of iron skarn deposits in the Southern Taihang district have been well studied [7,8,13]. In contrast, there are few researches about the iron skarn deposits in the Gujiao ore field. These studies reported zircon U–Pb age and geochemistry of the Huyanshan complex in the Gujiao ore field [14,15]. However, the geology and mineralization of iron skarn deposits have not been discussed in the previous papers. Furthermore, the ore-bearing monzonite implication to iron skarn mineralization is still not clear in the Gujiao ore field.

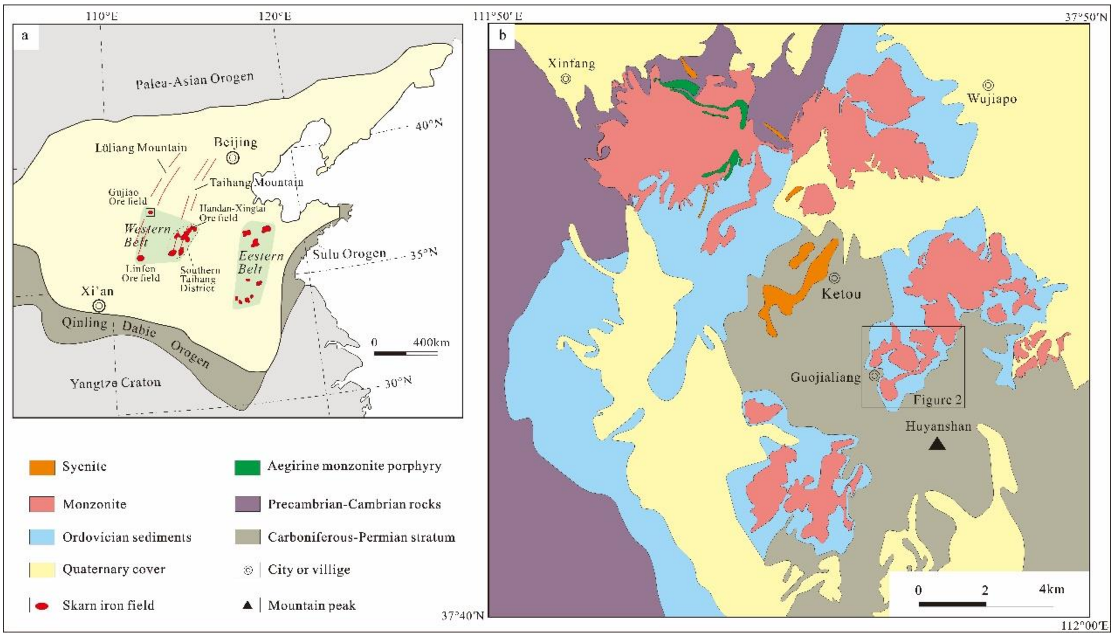


**Figure 1.** (**a**) Simplified geological map showing distribution of major iron skarn deposits in the North China Craton (NCC) (modified from [12]). (**b**) Geological map of the Gujiao ore field showing the distribution of the Huyanshan complex.

Mantle, continental crust materials, and oxidation state of magma play key role in formation of magmatic hydrothermal deposits such as porphyry copper, iron skarn, and porphyry molybdenum deposits, see, e.g., in [8,16–27]. Study of physico-chemical conditions of ore-bearing rocks is crucial to understand mineralization and to make metallogenic prognosis. The accessory mineral zircon is not only a conventional geochronological host for uranium and thorium; it is also widely used in revealing physico-chemical conditions of host rocks [18,22,25,28–30]. For example, the Ti concentration of zircon correlates with crystallization temperature [31], and Ce anomalies and Ce/Nd ratio reflect redox state of magma [29]. Sun et al. performed a contrastive study of zircons from ore-bearing and ore-barren plutons in the Handan-Xingtai district [8]. They concluded that the ore-bearing plutons had higher oxygen fugacity and lower temperature than ore-barren plutons. However, oxygen fugacity and temperature of the Gujiao ore-bearing monzonite are not studied yet. In this paper, the geological characteristics of the Guojialiang iron skarn deposit in the Gujiao ore field, and in situ zircon U–Pb dating results, and trace element composition of zircons from ore-bearing monzonites are presented. Geochemistry of ore-bearing rocks as well as ore mineralization age and the petrogenesis–metallogenic significance of intrusive rocks in the Gujiao ore field are discussed.

## 2. Geological Background

### 2.1. Ore Field Geology

The Gujiao iron skarn ore field, as one of the Mesozoic intraplate iron skarn fields in the western iron skarn deposit belt of NCC, is located in the middle segment of the Lüliang Mountain in central NCC (Figure 1a). The lithologies exposed in the Gujiao region are Precambrian metamorphic rocks, Cambrian sedimentary rocks, Ordovician carbonate rocks, Carboniferous-Permian coal-bearing sedimentary rocks, and Quaternary unconsolidated sediments (Figure 1b). The magmatic rocks are dominated by the Yanshanian period intrusive complex, Huyanshan complex, comprising monzonite, aegirine monzonite porphyry, and syenite. The complex outcropped ~50 $km^2$ and mainly intruded into the Ordovician carbonate sedimentary rocks (Figure 1b). The igneous rocks of the Huyanshan complex have intermediate $SiO_2$ contents, with high $Al_2O_3$, total alkali, Sr, and light rare earth elements (LREE) contents and low Y and heavy rare earth elements (HREE) contents [14]. These geochemical features of the Huyanshan complex are similar to those in the igneous complexes in the Handan-Xingtai district [32–34]. Skarns are distributed in the contact zone between monzonite and carbonate rocks. The iron skarn deposits are only associated with the monzonite in the Gujiao ore field. The zircon U–Pb dating of the Gujiao monzonites yielded 129.9 ± 2.3 Ma and 130 ± 3 Ma [14,15], which are consistent with the emplacement ages (136 to 129 Ma) of complexes in the Handan-Xingtai district [7,8,33,35,36].

## 2.2. Iron Deposit Geology

The Guojialiang deposit is located in the eastern Gujiao ore field. The exposed rocks are middle Ordovician carbonate rocks and Carboniferous-Permian paralic deposits. The middle Ordovician limestones were intruded by monzonites, which resulted in skarnization in the contact zone between limestone and monzonite, and marbleization of limestone near the intrusion rocks (Figure 2). The monzonite can be divided into two lithofacies by rock texture; one with equigranular texture as intrusive stock, and the other with porphyritic texture as apophysis. The transition of the textures between equigranular and porphyritic monzonite is gradual. The ore bodies mainly controlled by fold structure generally occur as lenticules in the contact zones between the limestone and monzonite apophysis as well as bedded veins in the limestone interlayers. In addition, some ore bodies occur in contact zones between limestone xenoliths and monzonite stock.

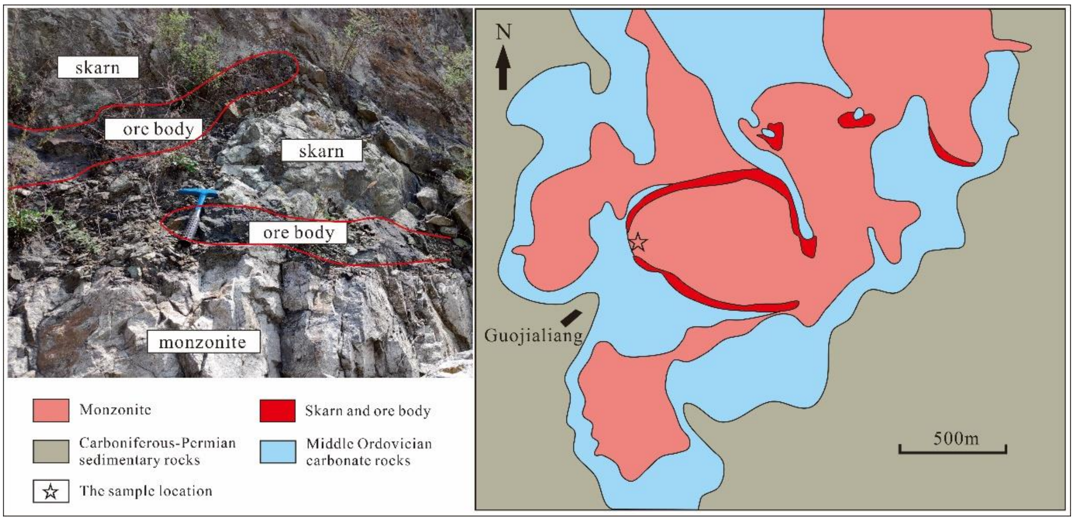


**Figure 2.** Geological map of the Guojialiang deposit showing iron skarn mineralization controlled by monzonite.

Hydrothermal alteration is well developed in the contact zones in both pluton and the surrounding limestone. The alteration zone can be divided into altered monzonite zone, endoskarn zone, exoskarn zone, and diopside-marble zone. The altered monzonite zone commonly occurs as lenticule and the intensity of alteration increases gradually from pluton to the country rocks. In the altered monzonite zone, feldspars are replaced by sericite, clay, and epidote; amphibole is replaced by albite and garnet; and sphene and garnet occur as hydrothermal minerals (Figure 3a). The endoskarn zone is comprised of garnet, diopside, and minor phlogopite and calcite. The exoskarn zone covers larger area than the endoskarn zone and mainly consists of diopside, phlogopite, and minor calcite and quartz. The diopside–marble zone is characterized by marbleization of limestone with local diopside near the exoskarn zone. Diopside skarn is dominated. Euhedral crystals of garnet and diopside are locally found in open spaces (Figure 3b,c). Iron ore bodies commonly occur as irregular masses in the endoskarn zone and as bedded veins in the marbleized limestone layers.

The Fe content of ore bodies ranges from 35 to 54 wt. %, with average of 45 wt. %. Phlogopite-magnetite and diopside-magnetite are two main ore types. The diopside-magnetite ore, with massive textures, consist of magnetite (25–40 vol. %), diopside (25–40 vol. %), phlogopite (10–15 vol. %), calcite (5–10 vol.

%), and specularite (0–5 vol. %) (Figure 3d). Phlogopite-magnetite ore includes magnetite (40–55 vol. %), phlogopite (30–40 vol. %), calcite (5–10 vol. %) and pyrite (~5 vol. %) (Figure 3e).

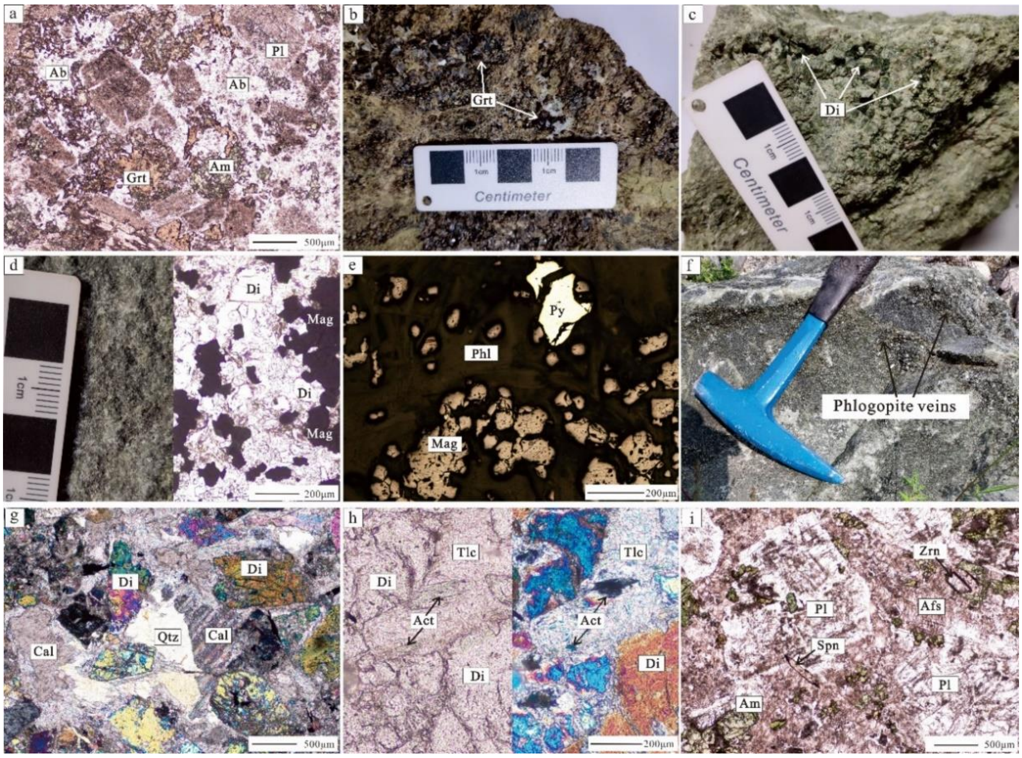


**Figure 3.** Petrography and microphotographs of the Guojialang deposits. (**a**) Altered monzonite showing feldspars, amphibole and garnet. (**b**,**c**) Euhedral garnet and diopside in open spaces. (**d**) Diopside-magnetite ore type. (**e**) Phlogopite-magnetite skarn ore type. (**f**) Phlogopite veins in diopside skarn. (**g**) Diopside overprinted by calcite and quartz. (**h**) Diopside replaced by actinolite; diopside and actinolite replaced by talc. (**i**) Monzonite texture and mineral relations. Ab—albite; Pl—plagioclase; Afs—alkali-feldspar; Am—amphibole; Grt—garnet; Di—diopside; Mag—magnetite; Py—pyrite; Phl—phlogopite; Cal—calcite; Qtz—quartz; Act—actinolite; Tlc—talc; Spn—sphene; Zrn—zircon.

Based on the petrographic observation, the metasomatism can be divided into four stages of skarn formation: prograde stage, retrograde stage, sulfide stage, and pneumatolytic stage. The prograde stage is dominated by garnet and diopside. The retrograde stage is characterized by phlogopite, actinolite and magnetite that replace garnet and diopside. Phlogopite veins in the diopside skarn are common (Figure 3f). A large volume of magnetite formed during the retrograde stage. The sulfide stage is weakly developed and formed calcite, quartz and pyrite, overprinting diopside and filling in pores of diopside (Figure 3g). The pneumatolytic stage is dominated by calcite, specularite, and talc. The diopside and actinolite is replaced by talc (Figure 3h).

## 3. Sample and Analytical Methods

Rock samples were collected from the monzonite in the northeast part of the Guojialiang village, Gujiao, China (GS01; 37°44′25″ N, 111°58′48″ E). The medium-grained and porphyritic monzonite is composed of plagioclase (40–50 vol. %), alkali-feldspar (35–40 vol. %), and hornblende (10–15 vol. %), with accessory zircon, apatite, sphene, and magnetite (Figure 3i).

Zircon grains were separated from the monzonite sample GS01 through a series of procedures, including crushing in a jaw crusher; desliming in water; density separation in dense liquid, magnetic separation; and, finally, handpicking under binocular microscope (United Scope LLC, Irvine, CA, USA). Zircon grains were then mounted in epoxy resin and polished. Cathodoluminescent images and transmitted /reflected microscopy were used to avoid fractures and inclusions and to select ablation locations in the zircon grains.

Zircon U–Pb dating was performed using a ThermoX2 inductively coupled plasma–mass spectrometry (ICP-MS) equipped with a GeoLas Pro 193 nm ablation system at the Testing Center of Shandong Bureau of China Metallurgical Geology Bureau, Jinan, China. The output laser energy density was fixed at 10 J/cm$^2$ and the ablation of laser was conducted at 6 Hz for 55 s after 25 s background acquisition. A spot diameter of 30 μm was conducted for all analyses. Helium was used as the carrier gas. The zircon 91500 was used as the external standard for U–Pb isotopic element ratio dating. The NIST SRM610 glass was used as external standard and $^{29}$Si as the internal standard to calibrate trace element concentrations. Offline data processing was conducted using the ICPMSDataCal software (version 10.8, China University of Geosciences, Wuhan, China) [37]. Uncertainties of individual analyses are reported with 2$\sigma$ errors. The plotting of concordia diagrams and weighted mean age calculations were performed using Isoplot/Ex_ver3 (version 3.0, Berkeley Geochronology Center, California, CA, USA) [38]. $^{206}$Pb/$^{238}$U age is accepted for zircons younger than 1000 Ma, whereas $^{206}$Pb/$^{207}$Pb age is reliable for zircons older than 1000 Ma.

Zircon Ti temperature calculation following the method described by Watson et al. [39] and used by Sun et al. [8] for the complexes in the Handan-Xingtai district. $Ce^{4+}/Ce^{3+}$ and $f O^2$ were calculated herein to imply oxygen state of monzonite. Zircon $Ce^{4+}/Ce^{3+}$ were estimated using the method described by Ballard et al. [22]. In lattice strain model, the La and Pr are often problematic due to their low concentrations in zircon; Eu and U are also not used for their multivalence issues [28,40]. The trace element contents of melt are replaced by whole rocks from Ying et al. [14]. The $f O^2$ were calculated using the calibration method from Smythe and Brenan [28]. The detail method is described in the Supplementary Document File S1. For comparison to iron deposits in the Handan–Xingtai district, the water content in ore-bearing magma of monzonite of Huyanshan complex is considered identical to that from ore-bearing magma in the Handan-Xingtai district (8.0 wt. %) [8].

## 4. Results

### 4.1. Zircon U–Pb Age

Zircon grains from monzonite (sample GS01) are commonly 100–200 μm in length and are light pink to colorless, euhedral, and prismatic. The Th and U contents in most zircons are high (from 1343 to 3937 ppm and from 1510 to 3090 ppm, respectively) except in the old inherited zircon (Table 1). The Th/U ratios vary from 0.51 to 1.55 indicating a magmatic source. Eleven analyses with good concordance (>90%) have $^{206}$Pb/$^{238}$U ages ranging from 126.2 to 135.2 Ma, with a weighted mean age of 129.7 ± 1.7 Ma (MSWD = 1.18, $n$ = 11; Figure 4). These ages are in agreement with those from Ying et al. [14] and Huo et al. [15]. The inherited zircon analyses show $^{207}$Pb/$^{206}$Pb ages ranging from 1773 to 2186 Ma, which is consistent with ages of the tectonic-magmatic event in the Lüliang district and event in the central NCC [41–43].

**Table 1.** LA-ICP-MS U–Pb data for zircons from the monzonite in the Guojialiang deposit.

| Spot | Th ppm | U ppm | Th/U | $^{207}$Pb/$^{206}$Pb | 2$\sigma$ | $^{207}$Pb/$^{235}$U | 2$\sigma$ | $^{206}$Pb/$^{238}$U | 2$\sigma$ | $^{207}$Pb/$^{206}$Pb Age (Ma) | 2$\sigma$ | $^{207}$Pb/$^{235}$U Age (Ma) | 2$\sigma$ | $^{206}$Pb/$^{238}$U Age (Ma) | 2$\sigma$ | Concordance |
|---|---|---|---|---|---|---|---|---|---|---|---|---|---|---|---|---|
| 1 | 2290 | 2547 | 0.90 | 0.0494 | 0.0021 | 0.1373 | 0.0070 | 0.0199 | 0.0005 | 168.6 | 100 | *130.7* | *6.2* | *127.1* | *3.0* | *97%* |
| 2 | 2421 | 2568 | 0.94 | 0.0576 | 0.0027 | 0.1625 | 0.0079 | 0.0202 | 0.0004 | 516.7 | 104 | 152.9 | 6.9 | 129.1 | 2.6 | 83% |
| 3 | 1480 | 1663 | 0.89 | 0.0557 | 0.0033 | 0.1489 | 0.0093 | 0.0192 | 0.0005 | 442.6 | 133 | 140.9 | 8.2 | 122.7 | 3.2 | 86% |
| 4 | 1343 | 1607 | 0.84 | 0.0556 | 0.0031 | 0.1573 | 0.0093 | 0.0203 | 0.0004 | 435.2 | 126 | 148.4 | 8.1 | 129.7 | 2.8 | 86% |
| 5 | 2331 | 2236 | 1.04 | 0.0581 | 0.0027 | 0.1609 | 0.0086 | 0.0198 | 0.0005 | 600.0 | 104 | 151.5 | 7.5 | 126.7 | 3.0 | 82% |
| 6 | 1994 | 1912 | 1.04 | 0.0540 | 0.0027 | 0.1482 | 0.0077 | 0.0198 | 0.0004 | 368.6 | 124 | *140.3* | *6.8* | *126.2* | *2.8* | *90%* |
| 7 | 2578 | 2334 | 1.10 | 0.0464 | 0.0021 | 0.1283 | 0.0059 | 0.0199 | 0.0004 | 16.8 | 122 | *122.6* | *5.3* | *127.3* | *2.6* | *96%* |
| 8 | 2084 | 1683 | 1.24 | 0.0515 | 0.0029 | 0.1459 | 0.0080 | 0.0205 | 0.0005 | 264.9 | 130 | *138.3* | *7.1* | *130.6* | *3.3* | *94%* |
| 9 | 2329 | 2145 | 1.09 | 0.0540 | 0.0026 | 0.1518 | 0.0078 | 0.0203 | 0.0005 | 372.3 | 117 | *143.5* | *6.9* | *129.4* | *3.1* | *90%* |
| 10 | 2828 | 2297 | 1.23 | 0.0560 | 0.0041 | 0.1506 | 0.0140 | 0.0192 | 0.0006 | 453.8 | 163 | 142.4 | 12.3 | 122.3 | 4.0 | 84% |
| 11 | 2308 | 1916 | 1.20 | 0.0604 | 0.0043 | 0.1724 | 0.0137 | 0.0204 | 0.0006 | 616.7 | 156 | 161.5 | 11.9 | 130.5 | 3.8 | 78% |
| 12 | 1944 | 2398 | 0.81 | 0.0483 | 0.0020 | 0.1416 | 0.0058 | 0.0212 | 0.0004 | 116.8 | 100 | *134.5* | *5.1* | *135.2* | *2.6* | *99%* |
| 13 | 2368 | 2090 | 1.13 | 0.0541 | 0.0029 | 0.1579 | 0.0086 | 0.0210 | 0.0004 | 376.0 | 113 | *148.8* | *7.6* | *134.1* | *2.7* | *90%* |
| 14 | 2368 | 2189 | 1.08 | 0.0498 | 0.0021 | 0.1377 | 0.0060 | 0.0199 | 0.0004 | 187.1 | 35 | *131.0* | *5.4* | *127.3* | *2.6* | *97%* |
| 15 | 84 | 138 | 0.60 | 0.1085 | 0.0049 | 4.5854 | 0.2592 | 0.3047 | 0.0111 | 1773.8 | 84 | 1746.6 | 47.1 | 1714.6 | 54.6 | 98% |
| 16 | 205 | 219 | 0.93 | 0.1324 | 0.0049 | 6.8924 | 0.2731 | 0.3757 | 0.0084 | 2129.3 | 63 | 2097.7 | 35.1 | 2055.9 | 39.2 | 97% |
| 17 | 247 | 483 | 0.51 | 0.1355 | 0.0044 | 7.2698 | 0.2573 | 0.3866 | 0.0079 | 2172.2 | 56 | 2145.1 | 31.6 | 2106.8 | 36.6 | 98% |
| 18 | 291 | 424 | 0.69 | 0.1364 | 0.0041 | 7.3884 | 0.2707 | 0.3898 | 0.0097 | 2183.3 | 54 | 2159.6 | 32.8 | 2121.7 | 45.0 | 98% |
| 19 | 2722 | 2452 | 1.11 | 0.0503 | 0.0020 | 0.1424 | 0.0058 | 0.0204 | 0.0004 | 209.3 | 93 | *135.2* | *5.1* | *130.2* | *2.7* | *96%* |
| 20 | 3937 | 3090 | 1.27 | 0.0543 | 0.0023 | 0.1518 | 0.0076 | 0.0201 | 0.0005 | 388.9 | 96 | *143.5* | *6.7* | *128.0* | *2.9* | *90%* |
| 21 | 1526 | 1510 | 1.01 | 0.0562 | 0.0027 | 0.1603 | 0.0077 | 0.0206 | 0.0005 | 461.2 | 117 | 151.0 | 6.7 | 131.5 | 3.1 | 86% |
| 22 | 103 | 66 | 1.55 | 0.1368 | 0.0061 | 6.8413 | 0.3343 | 0.3615 | 0.0110 | 2186.7 | 77 | 2091.1 | 43.3 | 1989.4 | 51.9 | 95% |
| 23 | 2168 | 2194 | 0.99 | 0.0522 | 0.0023 | 0.1491 | 0.0065 | 0.0205 | 0.0004 | 294.5 | 91 | *141.1* | *5.7* | *130.8* | *2.7* | *92%* |

Note: The analyses used to calculate average age are marked by italics.

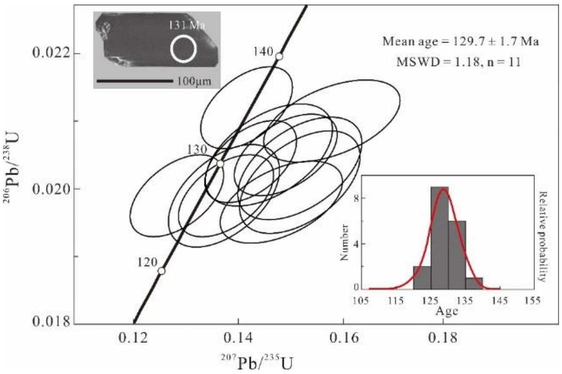


**Figure 4.** LA-ICP-MS zircon U–Pb concordia diagram of sample GS01 showing mean age for the monzonite.

## 4.2. Zircon Trace Elements

The studied zircons have high total REE concentration from 3614 ppm to 4782 ppm (Table 2), and they are enriched in HREE and depleted in LREE with outstanding positive Ce and weak negative Eu anomalies. The chondrite-normalized REE patterns show a left-leaning with Ce peak (Figure 5), implying a magmatic source [44]. It has been shown that high *Y* (>4433 ppm) and high total REE (>~3800 ppm) content are typical for zircons originated from monzonite [45]. The La concentrations of the zircons are mostly lower than 3 ppm, whereas the Lu concentrations are mostly higher than 370 ppm. The calculated Eu/Eu* [$Eu/Eu^* = Eu_N/(Sm_N \times Gd_N)^{1/2}$] and Ce/Ce* [$Ce/Ce^* = Ce_N/(La_N \times Pr_N)^{1/2}$] ratios from the eleven zircon analyses range from 0.60 to 0.72 and 23.38 to 45.85, respectively (Table 2).

**Table 2.** Trace elements of zircons with well concordance from monzonite and the results of temperature and oxygen fugacity in the Guojialiang ore deposit.

| No. | La | Ce | Pr | Nd | Sm | Eu | Gd | Tb | Dy | Ho | Er |
|---|---|---|---|---|---|---|---|---|---|---|---|
| 1 | 1.63 | 291.35 | 2.49 | 20.09 | 15.37 | 6.68 | 63.01 | 19.17 | 233.09 | 101.57 | 556.62 |
| 6 | 2.55 | 282.60 | 3.34 | 24.56 | 16.23 | 7.55 | 63.73 | 19.49 | 237.36 | 102.77 | 574.62 |
| 7 | 2.66 | 322.00 | 3.80 | 28.96 | 20.32 | 8.60 | 77.51 | 22.91 | 277.39 | 118.63 | 653.33 |
| 8 | 1.78 | 293.10 | 3.49 | 27.40 | 19.43 | 8.15 | 77.84 | 23.84 | 297.97 | 136.49 | 754.95 |
| 9 | 2.94 | 296.58 | 3.29 | 24.41 | 16.55 | 7.45 | 65.56 | 20.50 | 252.68 | 112.89 | 639.64 |
| 12 | 1.12 | 259.56 | 1.72 | 13.67 | 11.63 | 5.04 | 51.88 | 17.41 | 225.51 | 107.67 | 637.49 |
| 13 | 2.78 | 331.48 | 4.19 | 31.25 | 21.37 | 8.57 | 77.97 | 24.34 | 293.76 | 129.19 | 721.01 |
| 14 | 2.38 | 305.33 | 3.39 | 25.51 | 18.91 | 7.77 | 72.85 | 22.29 | 267.23 | 117.72 | 653.45 |
| 19 | 2.94 | 327.52 | 3.82 | 27.64 | 20.71 | 9.16 | 79.65 | 24.69 | 288.62 | 119.46 | 648.35 |
| 20 | 1.76 | 281.47 | 2.61 | 19.03 | 14.96 | 6.41 | 62.29 | 19.85 | 248.36 | 109.37 | 627.17 |
| 23 | 3.09 | 439.98 | 4.16 | 30.58 | 22.11 | 8.36 | 82.05 | 24.59 | 311.91 | 137.12 | 768.40 |
| **No.** | **Tm** | **Yb** | **Lu** | **Hf** | **Ti** | ***T*/°C** | **Eu/Eu*** | **Ce/Ce*** | **$Ce^{4+}/Ce^{3+}$** | **$\log fO_2$** | **ΔFMQ** |
| 1 | 151.15 | 1779.77 | 371.64 | 6957.23 | 2.82 | 641 | 0.66 | 35.46 | 218.20 | −15.36 | 3.43 |
| 6 | 153.73 | 1792.44 | 377.68 | 6603.01 | 3.27 | 651 | 0.72 | 23.74 | 173.92 | −14.97 | 3.52 |
| 7 | 176.44 | 1948.98 | 418.54 | 6534.23 | 3.36 | 653 | 0.66 | 24.83 | 154.14 | −14.83 | 3.6 |
| 8 | 201.46 | 2249.38 | 491.63 | 6072.93 | 5.80 | 695 | 0.64 | 28.83 | 169.38 | −13.73 | 3.53 |
| 9 | 171.16 | 1918.43 | 420.42 | 6366.11 | 5.51 | 691 | 0.69 | 23.38 | 193.80 | −13.90 | 3.47 |
| 12 | 176.20 | 2019.06 | 453.84 | 5887.37 | 4.81 | 680 | 0.63 | 45.85 | 385.27 | −14.21 | 3.45 |
| 13 | 192.46 | 2176.00 | 475.35 | 5779.29 | 7.25 | 713 | 0.64 | 23.81 | 156.82 | −13.09 | 3.70 |
| 14 | 175.36 | 1981.16 | 431.11 | 6217.55 | 2.82 | 641 | 0.64 | 26.36 | 175.35 | −15.16 | 3.63 |
| 19 | 167.62 | 1901.34 | 408.66 | 6463.16 | 4.81 | 680 | 0.69 | 23.96 | 154.72 | −14.14 | 3.53 |
| 20 | 169.06 | 1944.30 | 426.28 | 6086.94 | 7.68 | 700 | 0.64 | 32.20 | 213.10 | −13.21 | 3.92 |
| 23 | 203.10 | 2253.16 | 493.31 | 5805.57 | 6.16 | 718 | 0.60 | 30.09 | 245.93 | −13.25 | 3.41 |

Note: ΔFMQ denote the fayalite-magnetite-quartz buffer.

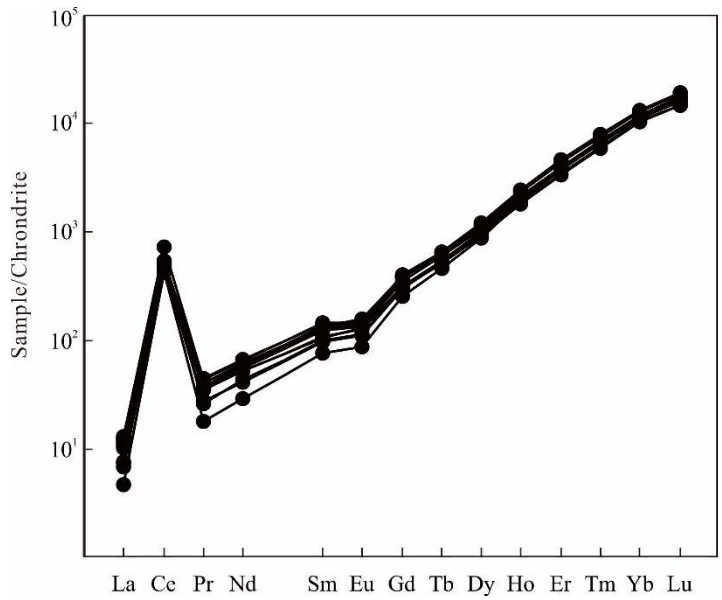


**Figure 5.** Chondrite-normalized REE patterns of zircon grains in monzonite from the Gujiao ore field.

### 4.3. Zircon Thermometer and Oxygen Meter

Zircon is widely used as thermometer and oxygen fugacity gauge in recent years [8,18,22,28,29,39,46,47]. Ti-in-zircon thermometer is a useful method to constrain magma temperature condition [31,48–50]. The Ti-in-zircon temperatures for eleven spots of zircon that has good concordance age from GS01 are in the range of 641 to 718 °C. The zircon oxygen-meter reflects the oxidation state of the source magma, where zircon crystallization is affected by several parameters such as Ce/Nd, $Ce^{4+}/Ce^{3+}$, and oxygen fugacity ($fO_2$) [8,21,28,29,47]. The calculated results of zircon $Ce^{4+}/Ce^{3+}$ ratios for sample GS01 varies from 154 to 385. The $fO_2$ ranges from −13.09 to −15.36 with an average $fO_2$ of ΔFMQ +3.6 (Table 2).

## 5. Discussion

### 5.1. Geochronology of the Ore Deposits

$^{40}Ar/^{39}Ar$ dating of phlogopite associated with skarn and U–Pb dating of hydrothermal allanite with ages of 137 ± 2 Ma and 136 ± 1 Ma, respectively, are coeval with zircon U–Pb ages of 136 ± 2 Ma from ore-bearing intrusions in the Handan-Xingtai district [13,51]. In addition, Deng et al. reported U–Pb ages of hydrothermal zircons from five major iron skarn deposits ranging from 133.6 to 128.5 Ma, which are consistent with U–Pb ages (134.1 to 128.5) of zircons from ore-bearing intrusions in each deposit in the Handan-Xingtai district [7]. These dates provide a robust correlation between the timing of the magmatism and mineralization, showing that the ages of ore deposits were identical to the ore-bearing intrusions. Our new age of 129.7 ± 1.7 Ma from zircon U–Pb dating is consistent with the zircon U–Pb age of 129.9 ± 2.3 Ma conducted by Ying et al. [14]. This shows that the Guojialiang iron skarn deposit formed around 129.7 Ma. The geochronology data suggests that the iron skarn deposits in western ore belt formed in the Early Cretaceous.

The inherited zircons may provide useful information on the genesis of magmas [52,53]. Inherited zircons, ~1800–2500 Ma in age, are commonly found in the ore-bearing intrusions from the Taiyuan ore field, Linfen ore field, and Handan-Xingtai district [8,13–15,35,51]. Not incidentally, ~1800–2500 Ma is a critical period of magmatic event and crustal growth in NCC [42,43,54]. The abundant zircons with Paleoproterozoic age in the ore-related plutons suggest that the ancient lower crustal materials played a key role in the magma genesis. This inference is further supported by Sr–Nd isotope data (Figure 6).

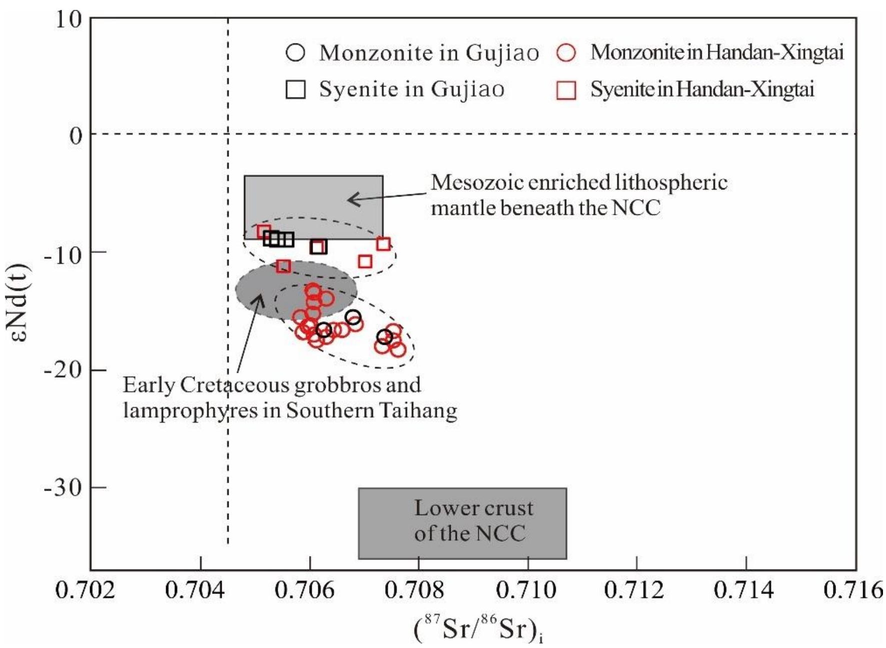


**Figure 6.** Sr–Nd isotope diagram for the syenitic-monzonitic intrusions from the western ore belt. The early Cretaceous enriched lithospheric mantle is constrained by uncontaminated basalt and Ordovician kimberlite in the eastern NCC [55–59]. The lower crust of NCC is from work in [60]. The early Cretaceous gabbros and lamprophyres in Southern Taihang area are given for comparison [9,61,62]. The monzonite and syenite from Gujiao after the work in [14] and Handan-Xingtai after the work in [34].

### *5.2. The Condition of Magma*

Trace element concentration in igneous zircons is shown to be sensitive to source rock type and crystallization environment [63]. Ti-in-zircon temperature may provide important evidence for the magmatic processes of crystallization. The monzonite in the Guojialiang ore deposit shows low Ti-in-zircon temperatures of 641–718 °C, which is slightly lower than the crystallization temperature of complexes in the Handan-Xingtai district. In addition, crystallization temperature of ore-bearing rocks was significantly lower than that of ore-barren plutons (Figure 7a).

The zircons from monzonite in the Guojialiang ore deposit have high Ce/Ce*, $Ce^{4+}/Ce^{3+}$, and log$fO_2$ values, which is similar to these from the ore-bearing rocks of the Handan-Xingtai district (Figure 7b,c) and also consistent with relatively high average oxygen fugacity of ΔFMQ+2.78. In contrast, the oxygen fugacity of ore-barren syenite ranges from ΔFMQ-3.34 to ΔFMQ-1.51 which is much lower than ore-bearing rocks (Figure 7d). Therefore, the ore-bearing magma had lower temperature and higher oxidation state compared to ore-barren magma. It is likely that the ore-bearing magmas were derived from an enriched lithospheric mantle with more crustal material contribution during ascend than that of the ore-barren magmas [8,32,34].

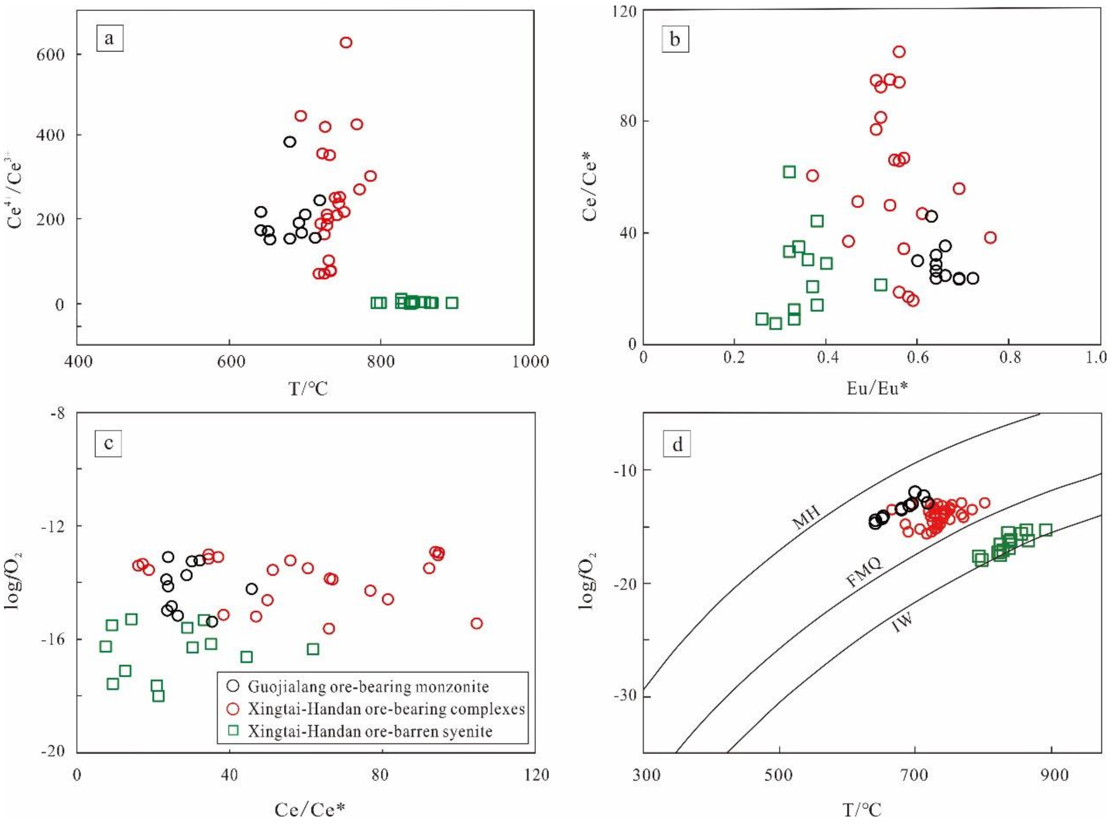


**Figure 7.** Ti-in-zircon temperature vs. zircon $Ce^{4+}/Ce^{3+}$diagram (**a**). Zircon Ce/Ce* vs Eu/Eu* diagram (**b**). Zircon Ce/Ce* vs log$fO_2$ diagram (**c**). Ti-in-zircon temperature vs log$fO_2$ diagram (**d**). The data of Handan-Xingtai district are from work in [8].

### 5.3. Implication for Mineralization

Zircon, as a common accessory mineral in natural rocks, is a robust indicator for many geological processes, such as crustal assimilation [64], crustal recycling [65], and metal concentrations [11]. Previous studies indicate that involvement of mantle materials can elevate iron contents of ore-related magma for formation of Fe skarn deposits [11]. Oxidation state of magmas could also be originally inherited from magma source and could be changed by magma processes such as crystallization, assimilation and mixing [66–68]. The inherited zircons and Sr–Nd isotope data suggest that the ore-bearing monzonite plutons likely formed by magma mixing from metasomatized mantle and crust, whereas ore-barren syenite plutons are derived from the metasomatized mantle with insignificant crustal contamination in the western Fe skarn ore belt (Figure 6) [8,14,34]. The zircon trace elements show that the oxygen fugacity of ore-bearing monzonite was much higher than ore-barren syenite (Figure 7). Thus, the high oxygen fugacity of monzonite magma can be probably attributed to ancient crustal materials [8]. $Fe^{3+}$ is more incompatible than $Fe^{2+}$ for most early crystalized minerals in magma (e.g., olivine and pyroxene). Under high $fO_2$ condition, such as ΔFMQ+1.2 to ΔFMQ+3, the $Fe^{3+}/Fe^{2+}$ ratio is high and sulfur in the magma occurs as sulfate, such as $SO_3^{2-}$ and $SO_4^{2-}$ rather than $S^{2-}$ [69]. Such conditions are needed to prevent Fe loss; otherwise, the $Fe^{2+}$ would combine with $S^{2-}$ to form insoluble FeS.

Metasomatic reactions in igneous-related hydrothermal fluids, such as diffusion and infiltration, are commonly major mechanisms for skarn formation [70,71]. Dissolution-assimilation is proposed as a mechanism for the formation of skarn deposits at Guojialiang. Euhedral diopside and garnet have been found in geodes from the diopside and garnet endoskarn zones. Assimilation of the country limestrone by post-magmatic hydrothermal fluid effectively promoted skarn formation. The Fe-enriched hydrothermal fluid caused metasomatic alteration and deposited ore along contact zones when the temperature decreased.

## 6. Conclusions

1. LA-ICP-MS zircon U–Pb dating suggests that the mineralization of the Guojialiang iron skarn deposit in the Gujiao ore field occurred at ~130 Ma, which is consistent with the timing of iron mineralization in the Handan-Xingtai district.

2. The ore-related monzonite in the Gujiao ore field, with high oxygen fugacity, Ce/Ce*, and $Ce^{4+}/Ce^{3+}$, had lower temperature and higher oxidation state compared to ore-barren magma.

3. Contribution of the crustal material to the magma source might have affected oxidation state of magma, which may be a critical factor for the iron mineralization in the western iron belt.

**Supplementary Materials:** The following are available online at http://www.mdpi.com/2075-163X/10/4/316/s1, File S1: Method for using zircon REE oxygen barometer and Ti thermometer.

**Author Contributions:** Data treatment and writing—original draft, Z.-G.C.; Review and editing, A.K.S. and G.-C.D.; Supervision and funding acquisition, G.-C.D. All authors have read and agreed to the published version of the manuscript.

**Funding:** This work is supported by the Ministry of Science and Technology of China (2016YFC0600106) and the National Natural Science Foundation of China (91755207, 41603063).

**Acknowledgments:** We gratefully acknowledge the two anonymous reviewers for the constructive comments that considerably improved the manuscript. We thank senior engineer Mingze Li at the Shanxi Provincial Geological Prospecting Bureau for his support in field work.

**Conflicts of Interest:** The authors declare no conflicts of interest.

## References

1. Zhu, R.X.; Yang, J.H.; Wu, F.Y. Timing of destruction of the North China Craton. *Lithos* **2012**, *149*, 51–60. [CrossRef]
2. Fan, W.M.; Zhang, H.F.; Baker, J.; Jarvis, K.E.; Mason, P.R.D.; Menzies, M.A. On and off the North China Craton: Where is the Archaean keel? *J. Petrol.* **2000**, *41*, 933–950. [CrossRef]
3. Menzies, M.; Xu, Y.; Zhang, H.; Fan, W. Integration of geology, geophysics and geochemistry: A key to understanding the North China Craton. *Lithos* **2007**, *96*, 1–21. [CrossRef]
4. Li, S.R.; Santosh, M. Geodynamics of heterogeneous gold mineralization in the North China Craton and its relationship to lithospheric destruction. *Gondwana Res.* **2017**, *50*, 267–292. [CrossRef]
5. Wu, F.Y.; Lin, J.Q.; Wilde, S.A.; Zhang, X.O.; Yang, J.H. Nature and significance of the Early Cretaceous giant igneous event in eastern China. *Earth Planet. Sci. Lett.* **2005**, *233*, 103–119. [CrossRef]
6. Zhu, R.X.; Zhang, H.F.; Zhu, G.; Meng, Q.R.; Fan, H.R.; Yang, J.H.; Wu, F.Y.; Zhang, Z.Y.; Zheng, T.Y. Craton destruction and related resources. *Int. J. Earth Sci.* **2017**, *106*, 2233–2257. [CrossRef]
7. Deng, X.-D.; Li, J.-W.; Wen, G. U–Pb Geochronology of hydrothermal zircons from the early cretaceous Iron Skarn Deposits in the Handan-Xingtai District, North China Craton. *Econ. Geol.* **2015**, *110*, 2159–2180. [CrossRef]
8. Sun, Y.; Wu, T.; Xiao, L.; Bai, M.; Zhang, Y. U–Pb ages, Hf–O isotopes and trace elements of zircons from the ore-bearing and ore-barren adakitic rocks in the Handan-Xingtai district: Implications for petrogenesis and iron mineralization. *Ore Geol. Rev.* **2019**, *104*, 14–25. [CrossRef]
9. Chen, B.; Zhai, M. Geochemistry of late Mesozoic lamprophyre dykes from the Taihang Mountains, north China, and implications for the sub-continental lithospheric mantle. *Geol. Mag.* **2003**, *140*, 87–93. [CrossRef]
10. Zhang, Z.; Hou, T.; Santosh, M.; Li, H.; Li, J.; Zhang, Z.; Song, X.; Wang, M. Spatio-temporal distribution and tectonic settings of the major iron deposits in China: An overview. *Ore Geol. Rev.* **2014**, *57*, 247–263. [CrossRef]
11. Meinert, L.; Dipple, G.; Nicolescu, S. World Skarn Deposits. In *Economic Geology 100th Anniversary Volume*; Society of Economic Geologists, Inc.: Littleton, CO, USA, 2005; pp. 299–336.
12. Duan, Z.; Li, J.-W. Zircon and titanite U–Pb dating of the Zhangjiawa iron skarn deposit, Luxi district, North China Craton: Implications for a craton-wide iron skarn mineralization. *Ore Geol. Rev.* **2017**, *89*, 309–323. [CrossRef]

13. Shen, J.F.; Santosh, M.; Li, S.R.; Zhang, H.F.; Yin, N.; Dong, G.C.; Wang, Y.J.; Ma, G.G.; Yu, H.J. The Beiminghe skarn iron deposit, eastern China: Geochronology, isotope geochemistry and implications for the destruction of the North China Craton. *Lithos* **2013**, *156*, 218–229. [CrossRef]
14. Ying, J.F.; Zhang, H.F.; Tang, Y.J. Crust-mantle interaction in the central North China Craton during the Mesozoic: Evidence from zircon U–Pb chronology, Hf isotope and geochemistry of syenitic-monzonitic intrusions from Shanxi province. *Lithos* **2011**, *125*, 449–462. [CrossRef]
15. Huo, T.; Yang, D.; Shi, J.; Xu, W.; Yang, H. Petrogenesis of the Early Cretaceous alkali-rich intrusive rocks in the central North China Block: Constraints from zircon U–Pb chronology and Sr–Nd–Hf isotopes. *Acta Petrol. Sin.* **2016**, *32*, 697–712. (In Chinese)
16. He, W.Y.; Mo, X.X.; Yang, L.Q.; Xing, Y.L.; Dong, G.C.; Yang, Z.; Gao, X.; Bao, X.S. Origin of the Eocene porphyries and mafic microgranular enclaves from the Beiya porphyry Au polymetallic deposit, western Yunnan, China: Implications for magma mixing/mingling and mineralization. *Gondwana Res.* **2016**, *40*, 230–248. [CrossRef]
17. Chen, J.; Xu, J.; Ren, J.; Huang, X. Late Triassic E-MORB-like basalts associated with porphyry Cu-deposits in the southern Yidun continental arc, eastern Tibet: Evidence of slab-tear during subduction? *Ore Geol. Rev.* **2017**, *90*, 1054–1062. [CrossRef]
18. Liang, H.-Y.; Campbell, I.H.; Allen, C.; Sun, W.-D.; Liu, C.-Q.; Yu, H.-X.; Xie, Y.-W.; Zhang, Y.-Q. Zircon $Ce^{4+}/Ce^{3+}$ ratios and ages for Yulong ore-bearing porphyries in eastern Tibet. *Miner. Depos.* **2006**, *41*, 152–159. [CrossRef]
19. Blevin, P.L.; Chappell, B.W. The role of magma sources, oxidation states and fractionation in determining the granite metallogeny of eastern Australia. *Trans. R. Soc. Edinb. Earth Sci.* **1992**, *83*, 305–316.
20. Ma, X.; Wang, Z.; Wang, C.; Yan, X. Crust-mantle magma mixing and implications for the formation of high Sr/Y ore-bearing porphyries in non-arc environments: A case study and discussion. *Acta Petrol. Sin.* **2014**, *30*, 2020–2030. (In Chinese)
21. Yao, L.; Lü, Z.; Zhao, C.; Pang, Z.; Yu, X.; Yang, T.; Li, Y.; Liu, P.; Zhang, M. Zircon U–Pb geochronological, trace element, and Hf isotopic constraints on the genesis of the Fe and Cu skarn deposits in the Qiman Tagh area, Qinghai Province, Eastern Kunlun Orogen, China. *Ore Geol. Rev.* **2017**, *91*, 387–403. [CrossRef]
22. Ballard, J.R.; Palin, M.J.; Campbell, I.H. Relative oxidation states of magmas inferred from Ce(IV)/Ce(III) in zircon: Application to porphyry copper deposits of northern Chile. *Contrib. Mineral. Petrol.* **2002**, *144*, 347–364. [CrossRef]
23. Sun, W.D.; Huang, R.F.; Li, H.; Hu, Y.B.; Zhang, C.C.; Sun, S.J.; Zhang, L.P.; Ding, X.; Li, C.Y.; Zartman, R.E.; et al. Porphyry deposits and oxidized magmas. *Ore Geol. Rev.* **2015**, *65*, 97–131. [CrossRef]
24. Zheng, Y.C.; Fu, Q.; Hou, Z.Q.; Yang, Z.S.; Huang, K.X.; Wu, C.D.; Sun, Q.Z. Metallogeny of the northeastern Gangdese Pb–Zn–Ag–Fe–Mo–W polymetallic belt in the Lhasa terrane, southern Tibet. *Ore Geol. Rev.* **2015**, *70*, 510–532. [CrossRef]
25. Qiu, J.T.; Yu, X.Q.; Santosh, M.; Zhang, D.H.; Chen, S.Q.; Li, P.J. Geochronology and magmatic oxygen fugacity of the Tongcun molybdenum deposit, northwest Zhejiang, SE China. *Miner. Depos.* **2013**, *48*, 545–556. [CrossRef]
26. Shu, Q.; Chang, Z.; Lai, Y.; Hu, X.; Wu, H.; Zhang, Y.; Wang, P.; Zhai, D.; Zhang, C. Zircon trace elements and magma fertility: Insights from porphyry (-skarn) Mo deposits in NE China. *Miner. Depos.* **2019**, *54*, 645–656. [CrossRef]
27. Jin, Z.; Zhang, Z.; Hou, T.; Santosh, M.; Han, L. Genetic relationship of high-Mg dioritic pluton to iron mineralization: A case study from the Jinling skarn-type iron deposit in the North China Craton. *J. Asian Earth Sci.* **2015**, *113*, 957–979. [CrossRef]
28. Smythe, D.J.; Brenan, J.M. Magmatic oxygen fugacity estimated using zircon-melt partitioning of cerium. *Earth Planet. Sci. Lett.* **2016**, *453*, 260–266. [CrossRef]
29. Trail, D.; Bruce Watson, E.; Tailby, N.D. Ce and Eu anomalies in zircon as proxies for the oxidation state of magmas. *Geochim. Cosmochim. Acta* **2012**, *97*, 70–87. [CrossRef]
30. Chapman, J.B.; Gehrels, G.E.; Ducea, M.N.; Giesler, N.; Pullen, A. A new method for estimating parent rock trace element concentrations from zircon. *Chem. Geol.* **2016**, *439*, 59–70. [CrossRef]
31. Watson, E.B.; Harrison, T.M. Zircon thermometer reveals minimum melting conditions on earliest Earth. *Science* **2005**, *308*, 841–844. [CrossRef]
32. Sun, Y.; Xiao, L.; Zhan, Q.; Wu, J.; Zhu, D.; Huang, W.; Bai, M.; Zhang, Y. Petrogenesis of the Kuangshancun and Hongshan intrusive complexes from the Handan-Xingtai district: Implications for iron mineralization

associated with Mesozoic magmatism in the North China Craton. *J. Asian Earth Sci.* **2015**, *113*, 1162–1178. [CrossRef]
33. Sun, Y.; Xiao, L.; Zhu, D.; Wu, T.; Deng, X.; Bai, M.; Wen, G. Geochemical, geochronological, and Sr–Nd–Hf isotopic constraints on the petrogenesis of the Qicun intrusive complex from the Handan–Xingtai district: Implications for the mechanism of lithospheric thinning of the North China Craton. *Ore Geol. Rev.* **2014**, *57*, 363–374. [CrossRef]
34. Chen, B.; Jahn, B.M.; Arakawa, Y.; Zhai, M.G. Petrogenesis of the Mesozoic intrusive complexes from the southern Taihang Orogen, North China Craton: Elemental and Sr–Nd–Pb isotopic constraints. *Contrib. Mineral. Petrol.* **2004**, *148*, 489–501. [CrossRef]
35. Li, S.-R.; Santosh, M.; Zhang, H.-F.; Shen, J.-F.; Dong, G.-C.; Wang, J.-Z.; Zhang, J.-Q. Inhomogeneous lithospheric thinning in the central North China Craton: Zircon U–Pb and S–He–Ar isotopic record from magmatism and metallogeny in the Taihang Mountains. *Gondwana Res.* **2013**, *23*, 141–160. [CrossRef]
36. Shen, J.F.; Li, S.R.; Santosh, M.; Dong, G.C.; Wang, Y.J.; Liu, H.M.; Peng, Z.D.; Zhang, Z.Y. Zircon U-Pb geochronology of the basement rocks and dioritic intrusion associated with the Fushan skarn iron deposit, southern Taihang Mountains, China. *J. Asian Earth Sci.* **2015**, *113*, 1132–1142. [CrossRef]
37. Liu, Y.S.; Hu, Z.C.; Zong, K.Q.; Gao, C.G.; Gao, S.; Xu, J.; Chen, H.H. Reappraisement and refinement of zircon U–Pb isotope and trace element analyses by LA-ICP-MS. *Chin. Sci. Bull.* **2010**, *55*, 1535–1546. [CrossRef]
38. Ludwig, K.R. *ISOPLOT 3.0: A Geochronological Toolkit for Microsoft Excel*; Special Publication No. 4; Berkeley Geochronology Center: Berkeley, CA, USA, 2003; Volume 4, pp. 1–71.
39. Watson, E.B.; Wark, D.A.; Thomas, J.B. Crystallization thermometers for zircon and rutile. *Contrib. Mineral. Petrol.* **2006**, *151*, 413–433. [CrossRef]
40. Zhang, C.C.; Sun, W.D.; Wang, J.T.; Zhang, L.P.; Sun, S.J.; Wu, K. Oxygen fugacity and porphyry mineralization: A zircon perspective of Dexing porphyry Cu deposit, China. *Geochim. Cosmochim. Acta* **2017**, *206*, 343–363. [CrossRef]
41. Liu, C.; Zhao, G.; Liu, F.; Shi, J. 2.2Ga magnesian andesites, Nb-enriched basalt-andesites, and adakitic rocks in the Lüliang Complex: Evidence for early Paleoproterozoic subduction in the North China Craton. *Lithos* **2014**, *208–209*, 104–117. [CrossRef]
42. Santosh, M.; Yang, Q.-Y.; Teng, X.; Tang, L. Paleoproterozoic crustal growth in the North China Craton: Evidence from the Lüliang Complex. *Precambrian Res.* **2015**, *263*, 197–231. [CrossRef]
43. Zhao, G.; Zhai, M. Lithotectonic elements of Precambrian basement in the North China Craton: Review and tectonic implications. *Gondwana Res.* **2013**, *23*, 1207–1240. [CrossRef]
44. Hoskin, P.W.O.; Schaltegger, U. The composition of zircon and igneous and metamorphic petrogenesis. In *Zircon*; Hanchar, J.M., Hoskin, P.W.O., Eds.; Reviews in Mineralogy and Geochemistry, Mineralogical Society of America: Chantilly, VA, USA, 2003; Volume 53, pp. 27–62.
45. Belousova, E.A.; Griffin, W.L.; O'Reilly, S.Y.; Fisher, N.I. Apatite as an indicator mineral for mineral exploration: Trace-element compositions and their relationship to host rock type. *J. Geochem. Explor.* **2002**, *76*, 45–69. [CrossRef]
46. Zou, X.; Qin, K.; Han, X.; Li, G.; Evans, N.J.; Li, Z.; Yang, W. Insight into zircon REE oxy-barometers: A lattice strain model perspective. *Earth Planet. Sci. Lett.* **2019**, *506*, 87–96. [CrossRef]
47. Chelle-Michou, C.; Chiaradia, M.; Ovtcharova, M.; Ulianov, A.; Wotzlaw, J.F. Zircon petrochronology reveals the temporal link between porphyry systems and the magmatic evolution of their hidden plutonic roots (the Eocene Coroccohuayco deposit, Peru). *Lithos* **2014**, *198*, 129–140. [CrossRef]
48. Moecher, D.P.; McDowell, S.M.; Samson, S.D.; Miller, C.F. Ti-in-zircon thermometry and crystallization modeling support hot Grenville granite hypothesis. *Geology* **2014**, *42*, 267–270. [CrossRef]
49. Cathey, H.E.; Nash, B.P.; Allen, C.M.; Campbell, I.H.; Valley, J.W.; Kita, N. U–Pb zircon geochronology and Ti-in zircon thermometry of large-volume low 6180 magmas of the Miocene Yellowstone hotspot. *Geochim. Cosmochim. Acta* **2008**, *72*, A143.
50. Sepidbar, F.; Mirnejad, H.; Ma, C. Mineral chemistry and Ti in zircon thermometry: Insights into magmatic evolution of the Sangan igneous rocks, NE Iran. *Chem. Erde-Geochem.* **2018**, *78*, 205–214. [CrossRef]
51. Deng, X.D.; Li, J.W.; Wen, G. Dating iron skarn mineralization using hydrothermal allanite-(La) U–Th–Pb isotopes by laser ablation ICP-MS. *Chem. Geol.* **2014**, *382*, 95–110. [CrossRef]
52. Keay, S.; Steele, D.; Compston, W. Identifying granite sources by SHRIMP U–Pb zircon geochronology: An application to the Lachlan foldbelt. *Contrib. Mineral. Petrol.* **1999**, *137*, 323–341. [CrossRef]

53. Torró, L.; Proenza, J.A.; Rojas-Agramonte, Y.; Garcia-Casco, A.; Yang, J.-H.; Yang, Y.-H. Recycling in the subduction factory: Archaean to Permian zircons in the oceanic Cretaceous Caribbean island-arc (Hispaniola). *Gondwana Res.* **2018**, *54*, 23–37. [CrossRef]
54. Zhao, G.; Sun, M.; Wilde, S.A.; Sanzhong, L. Late Archean to Paleoproterozoic evolution of the North China Craton: Key issues revisited. *Precambrian Res.* **2005**, *136*, 177–202. [CrossRef]
55. Yang, W.; Li, S. Geochronology and geochemistry of the Mesozoic volcanic rocks in Western Liaoning: Implications for lithospheric thinning of the North China Craton. *Lithos* **2008**, *102*, 88–117. [CrossRef]
56. Wu, K.; Ling, M.-X.; Sun, W.; Guo, J.; Zhang, C.-C. Major transition of continental basalts in the Early Cretaceous: Implications for the destruction of the North China Craton. *Chem. Geol.* **2017**, *470*, 93–106. [CrossRef]
57. Guo, P.; Niu, Y.; Sun, P.; Wang, X.; Gong, H.; Duan, M.; Zhang, Y.; Kong, J.; Tian, L.; Wu, S. The Early Cretaceous bimodal volcanic suite from the Yinshan Block, western North China Craton: Origin, process and geological significance. *J. Asian Earth Sci.* **2018**, *160*, 348–364. [CrossRef]
58. Geng, X.L.; Foley, S.F.; Liu, Y.S.; Wang, Z.C.; Hu, Z.C.; Zhou, L. Thermal-chemical conditions of the North China Mesozoic lithospheric mantle and implication for the lithospheric thinning of cratons. *Earth Planet. Sci. Lett.* **2019**, *516*, 1–11. [CrossRef]
59. Gao, S.; Rudnick, R.L.; Xu, W.L.; Yuan, H.L.; Liu, Y.S.; Walker, R.J.; Puchtel, I.S.; Liu, X.M.; Huang, H.; Wang, X.R.; et al. Recycling deep cratonic lithosphere and generation of intraplate magmatism in the North China Craton. *Earth Planet. Sci. Lett.* **2008**, *270*, 41–53. [CrossRef]
60. Jahn, B.M.; Wu, F.Y.; Lo, C.H.; Tsai, C.H. Crust-mantle interaction induced by deep subduction of the continental crust: Geochemical and Sr–Nd isotopic evidence from post-collisional mafic-ultramafic intrusions of the northern Dabie complex, central China. *Chem. Geol.* **1999**, *157*, 119–146. [CrossRef]
61. Wang, Y.; Fan, W.; Zhang, H.; Peng, T. Early Cretaceous gabbroic rocks from the Taihang Mountains: Implications for a paleosubduction-related lithospheric mantle beneath the central North China Craton. *Lithos* **2006**, *86*, 281–302. [CrossRef]
62. Zhang, H.; Liu, J.; Chen, Z.; Chen, B.; Peng, S.; Men, W. Petrogensis of the Pingshun complexes in the southern Taihang Mountains: Petrology, geochronology and geochemistry. *Geotecton. Metallog.* **2014**, *38*, 454–471.
63. Belousova, E.; Griffin, W.; O'Reilly, S.Y.; Fisher, N. Igneous zircon: Trace element composition as an indicator of source rock type. *Contrib. Mineral. Petrol.* **2002**, *143*, 602–622. [CrossRef]
64. Kemp, A.I.S.; Hawkesworth, C.J.; Foster, G.L.; Paterson, B.A.; Woodhead, J.D.; Hergt, J.M.; Gray, C.M.; Whitehouse, M.J. Magmatic and crustal differentiation history of granitic rocks from Hf–O isotopes in zircon. *Science* **2007**, *315*, 980–983. [CrossRef] [PubMed]
65. Van Kranendonk, M.J.; Kirkland, C.L. Orogenic climax of Earth: The 1.2–1.1 Ga Grenvillian superevent. *Geology* **2013**, *41*, 735–738. [CrossRef]
66. Richards, J.P. Magmatic to hydrothermal metal fluxes in convergent and collided margins. *Ore Geol. Rev.* **2011**, *40*, 1–26. [CrossRef]
67. Cao, M.J.; Qin, K.Z.; Li, G.M.; Evans, N.J.; McInnes, B.I.A.; Li, J.X.; Zhao, J.X. Oxidation state inherited from the magma source and implications for mineralization: Late Jurassic to Early Cretaceous granitoids, Central Lhasa subterrane, Tibet. *Miner. Depos.* **2018**, *53*, 299–309. [CrossRef]
68. Hattori, K.H.; Keith, J.D. Contribution of mafic melt to porphyry copper mineralization: Evidence from Mount Pinatubo, Philippines, and Bingham Canyon, Utah, USA. *Miner. Depos.* **2001**, *36*, 799–806. [CrossRef]
69. Konecke, B.A.; Fiege, A.; Simon, A.C.; Parat, F.; Stechern, A. Co-variability of $S^{6+}$, $S^{4+}$, and $S^{2-}$ in apatite as a function of oxidation state: Implications for a new oxybarometer. *Am. Mineral.* **2017**, *102*, 548–557. [CrossRef]
70. Brown, P.E.; Essene, E.J. Activity variations attending tungsten skarn formation, Pine Creek, California. *Contrib. Mineral. Petrol.* **1985**, *89*, 358–369. [CrossRef]
71. Meinert, L.D. Skarns and skarn deposits. *Geosci. Can.* **1992**, *19*, 145–162.